

In situ Raman spectroscopy of MgSiO₃ enstatite up to 1550 K

RACHEL ZUCKER AND SANG-HEON SHIM*

Department of Earth, Atmospheric, and Planetary Sciences, Massachusetts Institute of Technology, Cambridge, Massachusetts 02139, U.S.A.

ABSTRACT

Significantly reduced detection of thermal radiation in gated spectroscopy allowed us to measure the Raman scattering of natural enstatite up to 1550 K at 1 bar. The intrinsic anharmonicity, $a_i = [(\partial \ln \nu_i)/(\partial T)]_v$, of the Raman-active modes in orthoenstatite (OEn) was obtained from temperature (T) shifts of vibrational frequencies measured in this study combined with previous high-pressure (P) Raman scattering data. Although the a_i values of the lattice modes of OEn are similar to those for forsterite (Fo), the Si-O stretching modes have significantly lower intrinsic anharmonicity in OEn than in Fo, suggesting that the connectivity of the SiO₄ tetrahedra plays an important role in mode anharmonicity. At the phase transition at 1500 K, a doublet related to the stretching vibration of bridging O atoms in the SiO₃ chains becomes a singlet, and a doublet related to the stretching vibration of non-bridging O atoms remains as a doublet, consistent with the expected spectral change for a phase transition from OEn to protoenstatite. Two intense, low-frequency modes of OEn show a strong nonlinear decrease in frequencies with heating that cannot be explained solely by thermal expansion. This may indicate the reorganization of the structure around Mg atoms and unkinking of the SiO₃ chains at temperatures well below the phase transition.

Keywords: Raman spectroscopy, gated spectroscopy, orthoenstatite, protoenstatite, phase transition, high temperature

INTRODUCTION

Magnesium-rich pyroxene (Mg,Fe)SiO₃ composes approximately 40% of the Earth's upper mantle (Ringwood 1975). Therefore, a comprehensive understanding of the thermal properties and phase transitions of pyroxene under geologic conditions is important.

The pressure-volume-temperature (P - V - T) equations of state for mantle minerals are fundamental to understanding the composition and dynamics of the mantle in the context of seismic data (Knittle and Jeanloz 1987; Stixrude et al. 1992; Ita and Stixrude 1992). Gillet et al. (1997) showed that the volume and temperature dependence of the intrinsic anharmonicity is important to consider for the thermal part of the equation of state. Because the mantle temperature is expected to be very high, $T > 1500$ K, constraining anharmonicity for mantle minerals is important. However, only a few measurements exist for anharmonicity of mantle minerals [e.g., forsterite (Fo) (Gillet et al. 1993, 1997)], and the anharmonicity of (Mg,Fe)SiO₃-pyroxene has not yet been measured.

MgSiO₃ undergoes many phase transitions during heating and compression. The most abundant low- T phase of En is orthoenstatite (OEn), with an orthorhombic unit cell in space group *Pbca*. MgSiO₃ undergoes a phase change around 1300 K (Smyth 1974; Yang and Ghose 1995; Jackson et al. 2004). X-ray diffraction (XRD) studies have revealed that the SiO₃ chains unkink drastically and tilt during this transformation, and the M2-O bond distance increases (M2 is the larger Mg site) (Yang and Ghose

1995); this high- T phase is protoenstatite (PEn). There are also reports of a phase transition to clinoenstatite (CEn) above 1500 K (Perrotta and Stephenson 1965) (hereafter HTCEn), which has a distinctly different structure from low- T CEn (LTCEn), but it appears that the occurrence of HTCEn may be related to shear stress or other non-equilibrium conditions (Shimobayashi and Kitamura 1993).

A Brillouin spectroscopy study reported severe softening of some single-crystal elastic moduli at temperatures well below that of the phase transition (Jackson et al. 2004). Considering that elastic softening below a transition T can lead to a displacive transition, Jackson et al. (2004) proposed the possible existence of a new phase with a *Cmca* structure in the phase diagram of MgSiO₃ at high T . They further proposed, however, that because of the reconstructive OEn → PEn transition at similar T , the system does not undergo a transition to the *Cmca* phase. A recent molecular dynamics simulation proposed that OEn may undergo an isosymmetric phase transition at ~1000 K (Miyake et al. 2004), which is related to the unkinking of the SiO₃ chain and the rearrangement of bonds between Mg in the M2 site and oxygen atoms. However, the actual existence of such an isosymmetric phase transition has yet to be confirmed in MgSiO₃.

Raman spectroscopy is a standard laboratory tool for studying minerals and materials (e.g., McMillan and Hofmeister 1988; Gillet et al. 1998; Weber and Merlin 2000; Eremets 1996). It provides structural information. Furthermore, changes in Raman mode frequencies with heating combined with high- P Raman measurements provide opportunities to measure intrinsic anharmonicity (Gillet et al. 1989, 1991, 1997).

A single spectrum of the high- T phase of MgSiO₃ was

* E-mail: sangshim@mit.edu

measured at 1050 K by Sharma (1989). Another conventional dispersive-Raman study reported room- T spectra of metastably water-quenched PEn crystals and in situ high- T spectra of PEn up to 1540 K (Reynard et al. 2008). However, these studies were performed for phase identification and do not provide sufficient information on the high- T spectral behaviors of MgSiO₃-OEn. In addition, acquiring high-quality, in situ, high- T measurements of Raman scattering has been difficult due to the interference with intense thermal radiation from the sample at high T in conventional Raman experiments (Laserna 1996).

One of the most effective ways to reduce the detection of thermal radiation is to synchronize a pulsed laser beam with a gated detector, i.e., gated spectroscopy (Bernardez et al. 1992; Exarhos and Schaaf 1991; Fayette et al. 1994; Herchen and Cappelli 1991; McCarty 1990; Simon et al. 2003; Goncharov and Crowhurst 2005). With the presence of other random error sources, the following equation describes an improvement in the signal-to-background ratio, SBR , expected for a gated spectroscopy setup (Mulac et al. 1978):

$$SBR_p = \frac{r}{f\Delta} \frac{P_p}{P_{CW}} SBR_{CW} \quad (1)$$

where r is the fraction of the pulsed power contained within the gate duration, f is the pulse repetition frequency, and Δ is the gate width. P_p and P_{CW} are the average power of a pulsed laser and the power of a continuous-wave (CW) laser, respectively, with the same wavelengths. This equation shows that SBR can be increased by decreasing the gate width, Δ , and the pulse repetition frequency, f .

We have developed a nanosecond gated spectroscopy system to measure Raman scattering in situ at high T (Slotznick and Shim 2008). This system allows us to measure changes in the vibrational frequencies of OEn during heating up to 1550 K at 1 bar. This data set provides quantitative information on the anharmonicity of Raman-active modes in OEn and insights into the crystal structure of the high- T phase of enstatite.

EXPERIMENTAL METHODS

Design of nanosecond gated Raman system

To achieve gating, a frequency-doubled Nd:YLF laser ($\lambda = 526.5$ nm, diode-pumped, Q-switched, Photonics Industries, Inc.) is synchronized with an intensified, gated CCD detector (PI-MAX, Princeton Instruments). We use a pulse repetition rate of 1 kHz with a pulse duration of 20 ns (Laser in Fig. 1). An average power of 10–40 mW is sufficient to obtain $SBR > 1000$ for typical oxides and silicates without inducing surface damage. The intensified, gated CCD detector (IGCCD attached to SP in Fig. 1) has a quantum efficiency of 30–40% for a range of 480–700 nm where most Raman measurements are performed. The CCD provides approximately 1 cm⁻¹ resolution for an 1800 grooves/mm grating.

The power of laser pulses is controlled by a wave plate combined with a polarizing beam splitter (PBS in Fig. 1). Only vertically polarized laser pulses, which are reflected by the beam splitter, are selected for Raman scattering. The pulse is then reflected by a holographic bandpass filter, which suppresses laser plasma lines. The pulse is further split 50:50 by a non-polarizing beamsplitter (BS1 in Fig. 1), with half the intensity of the pulse measured by an on-line laser power meter for monitoring laser power during Raman measurements.

To accept a wide range of sample forms, the system was built with two separate sample stages for vertical and horizontal laser beam incidence. For the diamond-anvil cell, horizontal beam incidence is preferred for double-sided laser heating. For a micro-heating stage, vertical beam incidence is preferred because it allows the samples to be placed at the bottom of the heater, which is the farthest

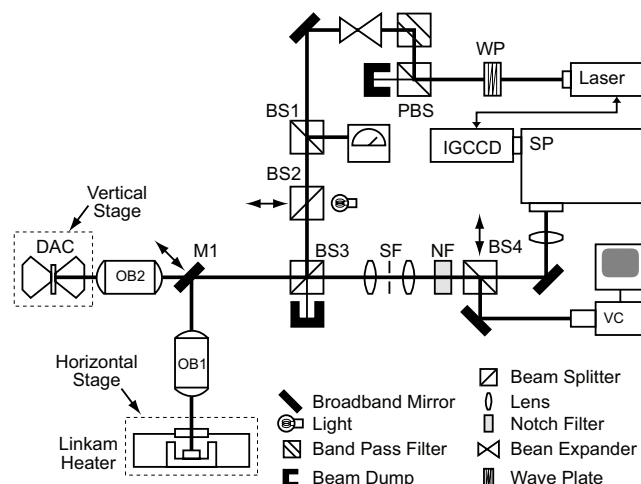


FIGURE 1. A schematic diagram of a gated Raman spectroscopy system combined with a micro-heating stage (used in this study) and a diamond-anvil cell (not used in this study). Laser = pulsed Nd:YLF laser ($\lambda = 526.5$ nm) for the excitation of Raman scattering, SP = 500 mm focal length single spectrometer for Raman spectroscopy, IGCCD = intensified gated CCD detector, DAC = diamond-anvil cell, OB1–2 = objective lenses, NF = notch filter, BS1–4 = beam splitters, M = mirror, SF = spatial filter, PBS = polarizing beam splitters, and VC = video camera. Movable optical components are shown with arrows.

from the cold cell window.

The objective lenses focus the laser pulses and collect Raman scattering from the sample (OB1 and OB2 in Fig. 1). Using a beam expander (Fig. 1), the size of laser focus on the sample surface is adjusted to 10–20 μm . Half of the Raman scattering intensities collected by an objective lens pass through a beam splitter (BS3 in Fig. 1), which allows for back-scattering measurements collected with OB1. A spatial filter is installed to reject stray light and signals from unwanted components of the pressure or temperature cell (i.e., a confocal setup), such as window materials. The depth of field of approximately 50–100 μm is sufficient to significantly reduce the signal from window materials of the pressure or temperature cell. A holographic super-notch filter (Kaiser optics) (LaPlant et al. 1996) in front of the spectrometer rejects the Rayleigh lines. A beamsplitter on a rail (BS4 in Fig. 1) can be inserted in the beam path to direct the sample image to a video camera.

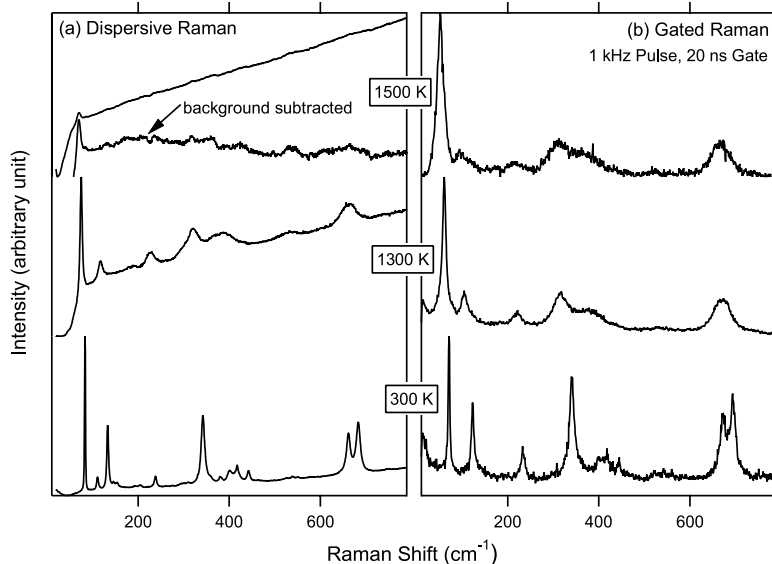
A commercially available micro-heating stage is used for heating at ambient pressure (TS1500, Linkam Scientific Instruments). A thermocouple attached directly to the micro-furnace in the heating stage measures temperature. Temperature can be regulated within ± 1 K (TMS94/1500, Linkam Scientific Instruments) by a feedback system connected to a thermocouple reader and a power supply. Pure argon gas flows through the heating chamber at high T to prevent oxidation of heating elements and the samples during heating.

Performance of the nanosecond gated spectroscopy system

To examine the improvement in SBR of Raman spectra obtained by the gating technique, we compare Raman scattering of En measured using conventional dispersive and gated techniques at 300–1500 K and 1 bar (Fig. 2). For measurements with a dispersive setup, we used the 514.5 nm beam of an Ar/Kr mixed ion CW laser combined with a back-illuminated CCD detector (Shim et al. 2007; Catalli et al. 2008; Hustoft et al. 2008).

Due to the superior sensitivity and resolution of the back-illuminated CCD detector, the dispersive technique allows us to resolve many more features (particularly weak intensity peaks) with smaller peak widths at room T compared with the gated setup (Fig. 2). With an increase of T , however, the background increases in the spectrum from the dispersive setup, whereas the background remains essentially the same in the spectra from the gated setup. In the spectra from both the dispersive and gated setups, the peak widths increase with T due to the thermal effect.

At 1500 K, the spectrum from the dispersive setup is completely dominated by the thermal radiation from the sample. Even after background subtraction from



◀ **FIGURE 2.** Raman spectra of $\text{MgSiO}_3\text{-En}$ at 300, 1300, and 1500 K measured with (a) a dispersive-Raman system with a 514.5 nm CW laser beam and (b) a gated Raman system with a 526.5 nm pulsed laser beam. We present raw spectra except for the background subtracted dispersive Raman spectrum at 1500 K shown together with the raw spectra.

a polynomial fit, only the most intense peaks can be reliably resolved because of noise from thermal radiation. In contrast, our gated setup successfully resolves even weak peaks at high T with the background remaining low and flat. The *SBR* of both spectra calculated from an intense peak at 85 cm^{-1} shows that our gated setup enhances the *SBR* by a factor of 2000 at 1500 K.

Temperature calibration via Raman thermometry

The temperature of materials can be calculated from the intensities and frequencies of the Stokes and anti-Stokes scattering of a phonon, i.e., Raman thermometry. The number of molecules in each state at a given temperature is governed by the Boltzmann distribution (LaPlant et al. 1996):

$$\frac{I_a}{I_s} = \frac{(v_0 - v_1)^4}{(v_0 + v_1)^4} \exp\left(\frac{-hv_1c}{kT}\right) \quad (2)$$

where v_0 is the frequency of excitation source and v_1 is the vibrational frequency; I_a and I_s are anti-Stokes and Stokes intensities, respectively; c is the speed of light, h is the Planck constant, and k is the Boltzmann constant.

We have measured the Stokes and anti-Stokes intensities of the first-order Raman modes of diamond up to 1073 K. Diamond is chosen because of its high thermal conductivity and intense first-order Raman mode at 1330 cm^{-1} . Diamonds are held at constant temperature in the heater for at least 5 min before each measurement to allow them to equilibrate to the new T . The sensitivity of the detector varies with wavelength. To account for this, we obtained a correction factor for the intensity ratio from Raman measurements at room T . A systematic offset was found between the T measured using Raman thermometry (“True Temperature” in Fig. 3) and the T read from the thermocouple (“Measured Temperature” in Fig. 3).

To confirm the trend observed in Raman thermometry, the melting T of gold was measured in the same heater by inspecting changes in surface texture through a video microscope attached to the gated spectroscopy system. The melting T of gold was found to be 1387 K, which is higher than the reported melting T by 50 K. This confirms a systematic overestimation of T as found by our Raman thermometry. As shown in Figure 3, the extrapolation of the linear fit for the trend observed in Raman thermometry of diamond successfully explains the T offset observed in the melting T of gold. The systematic overestimation of T perhaps results from thermal gradients between the locations of thermocouple and the sample in the heater. In this study, we correct the measured T using the results shown in Figure 3.

Sample

Natural, gem-quality OEn from Mogok, Burma, was used. Electron microprobe analysis showed that it is pure MgSiO_3 , with no detectable impurities. The crystal of OEn was broken into pieces 1–3 mm in size. The pieces that were nearest to euhedral were selected for Raman study.

The Raman spectrum from OEn varies with crystallographic orientation. We aligned the crystals to the orientation where a peak at 85 cm^{-1} , n_1 , can be

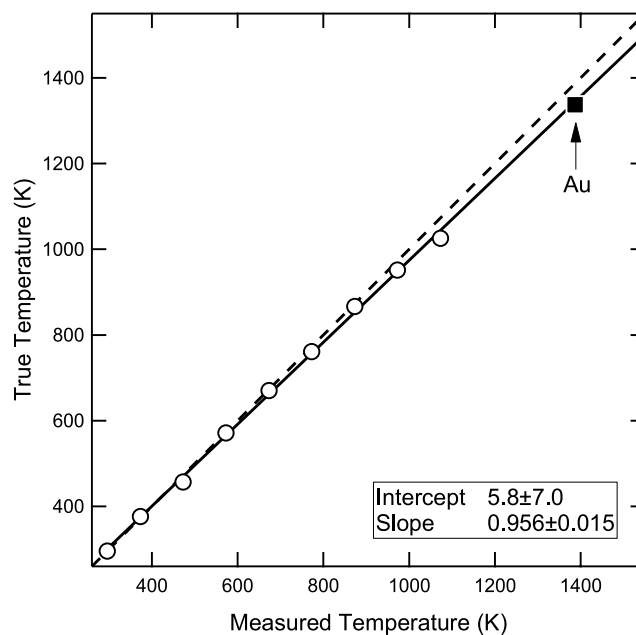


FIGURE 3. Temperature reading from TMS94/1500 controller (“measured temperature”) and temperature calculated from Raman thermometry (“true temperature”). The melting temperature of gold was also measured in the Linkam TS1500 heater (solid square). Systematic offsets were found between the temperature reading from the TMS94/1500 controller and the Raman thermometry. The linear fit of the data for temperature correction is shown.

maximized. However, not all the spectra are the same and two distinct groups of spectra are identified: the crystals used in runs 2 and 5 resemble single-crystal Raman spectra in *zz* polarization for A_{1g} symmetry (Fig. 4), and the crystals used in run 4 resemble single-crystal Raman spectra in *xx* polarization for A_{1g} symmetry (Fig. 5) (Chopelas 1999).

High-temperature Raman measurements

At elevated T , we accumulated 200 000 spectra over 200 s. Focus was readjusted after each T increase. Video imaging was used to make sure the sample was not damaged due to the intensity of the laser pulse every 100 K. A total of 5 separate heating runs were made. From these, we present runs 2, 4, and 5 because they

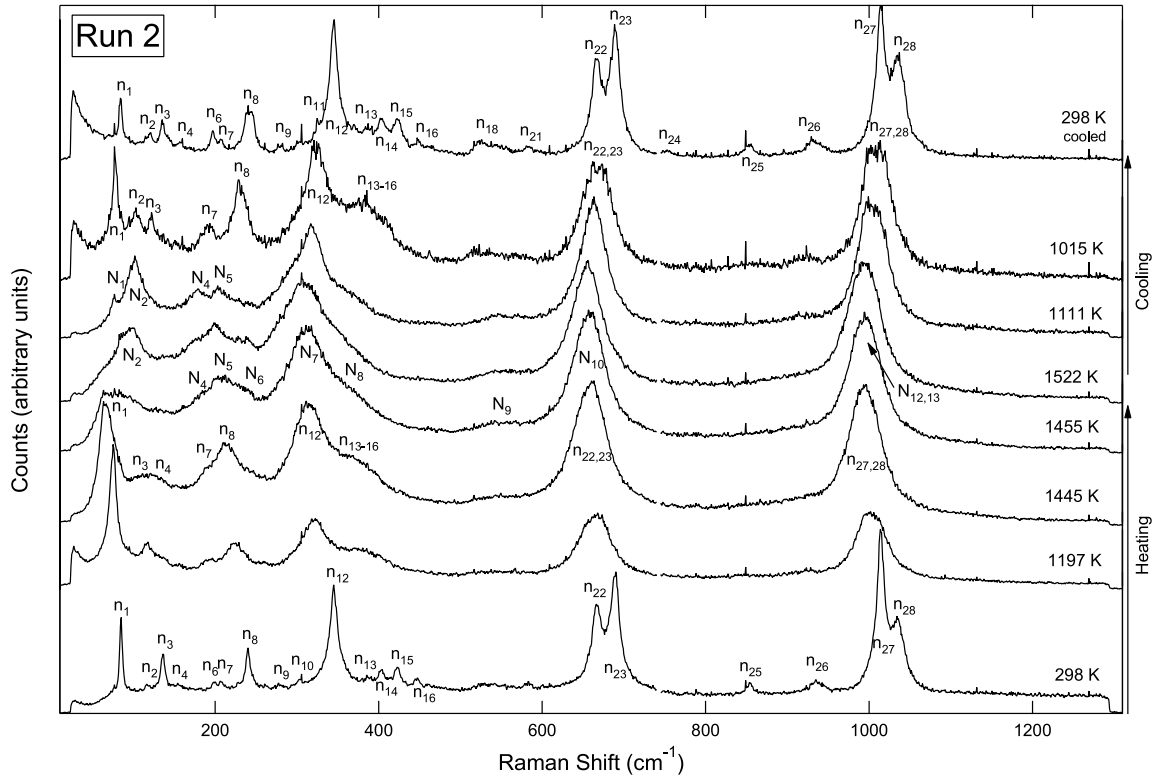


FIGURE 4. High-temperature Raman spectra of $\text{MgSiO}_3\text{-En}$ measured in run 2. The peaks are labeled in order of their frequencies. The peaks from low- and high- T phases are labeled as n_i and N_i , respectively. Presented are raw Raman spectra without background subtraction.

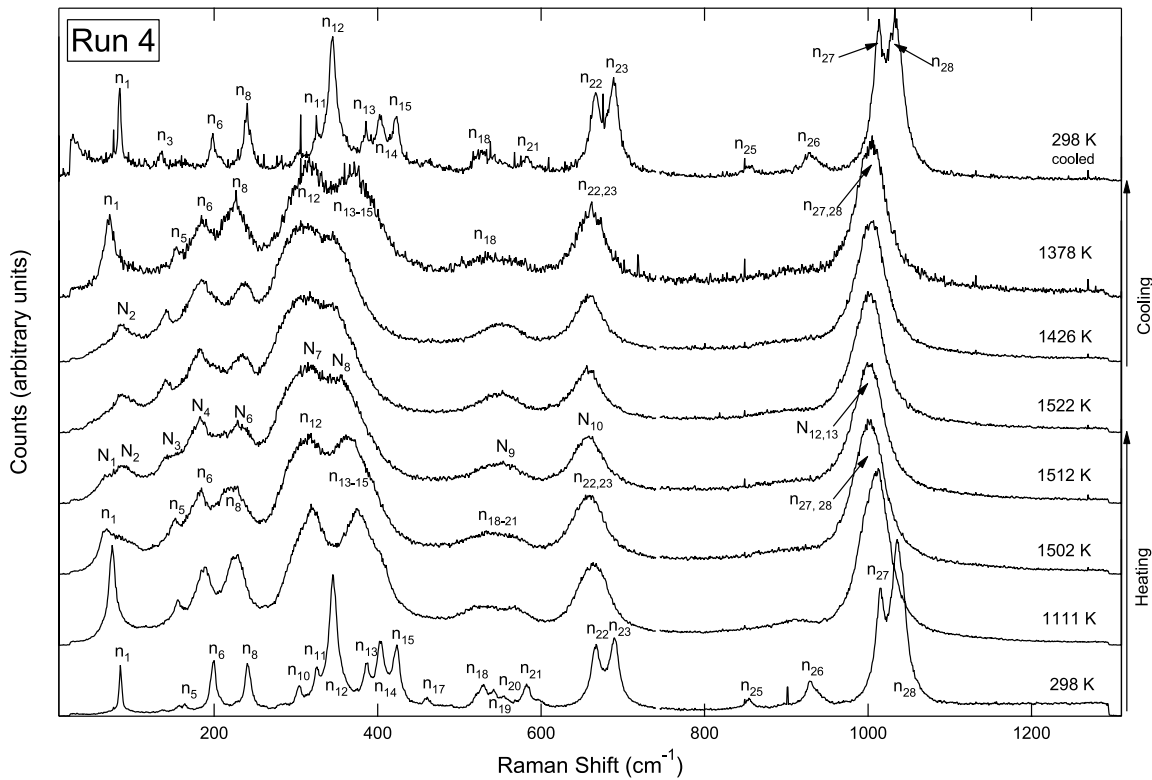


FIGURE 5. High-temperature Raman spectra of $\text{MgSiO}_3\text{-En}$ measured in run 4. The notations are the same as those in Figure 4.

show higher quality spectra.

Temperature was increased at a rate ranging from 5 to 10 K/min. The sample was held at the new T for about 3 min to equilibrate before measurements began. We measured spectra right after arriving at the target T , and then at 5 min and at 2 h, while holding the temperature. All three of these spectra are indistinguishable, so it can be assumed that the sample reaches the target T immediately. After the cooling measurements, the furnace was turned off at about 330 K and the sample was allowed to cool to room T overnight. The final room- T spectrum was measured on the following day.

RESULTS

Raman scattering of OEn at high T

Group theory predicts a total of 120 Raman-active phonon modes for OEn (Chopelas 1999). We observed a total of 28 modes at ambient conditions (Figs. 4 and 5). This is mainly because of the lower sensitivity of the gated detector for low-intensity features and higher electrical noise of the amplifier in the gated detector. Our dispersive-Raman spectrometer detected many more features for the same sample (Fig. 2). By comparison with polarized Raman spectra, 24 of these were found to be within 3 cm^{-1} of modes previously observed in A_{1g} symmetry (Choudhury et al. 1998; Chopelas 1999). The three remaining modes, 116 (n_2), 460 (n_{17}), and 582 (n_{21}) cm^{-1} , were found only in B_{1g} symmetry (Choudhury et al. 1998; Chopelas 1999).

By comparison with room- T Raman spectra reported by Lin (2004) for LTCEn and OEn, our samples were identified as OEn. OEn shows a strong mode at 85 cm^{-1} , whereas the lowest frequency mode for LTCEn is at 120 cm^{-1} . Our En sample shows the strong mode at 85 cm^{-1} and lacks the LTCEn feature at 120 cm^{-1} .

Upon heating, the Raman peaks broaden, but the background remain essentially the same as at ambient T , which demonstrates the effectiveness of the gating technique. For well-resolved Raman-active modes, we fit T -induced frequency (ν_i) changes to the following polynomial equation:

$$\nu_i(V, T) = \nu_{0K} + A_T T + B_T T^2. \quad (3)$$

The results are presented in Figure 6 and Table 1.

As mentioned above, slight differences in the orientations of the crystals in different runs result in different spectral intensities for the Raman modes. For example, the frequency of n_3 is more accurately determined in run 2 and 5, whereas that of n_5 is better determined in run 4. For n_1 we found that the T -induced frequency shift is smaller in run 4 than in other runs. This could have been because the sample in run 4 was not centered over the thermocouple and was at a cooler place within the furnace. In addition, the argon flow rate for run 4 was slightly higher than for other runs, which might have cooled the sample surface and made the sample T lower than the thermocouple reading. It is also worth mentioning that the sample used in run 4 undergoes the phase transformation at much higher T . Therefore, except for the modes that are observed only in run 4, we used results from runs 2 and 5 for the frequency fitting (Table 1).

Most vibrational modes of OEn show linear decreases in frequency with heating (Table 1) except for the n_1 and n_3 modes (Fig. 6). The rate of T -induced frequency shift ($A_T = d\nu/dT$) is similar among these modes and also similar to those for the Ra-

man-active modes in forsterite (Fo) (Gillet et al. 1997). However, in Fo, no modes showed such a pronounced non-linear decrease in frequency as we found for n_1 and n_3 in OEn.

Combined with the P -induced frequency (ν_i) shifts (Chopelas 1999; Lin 2003) and the analytical method proposed by Gillet et al. (1997), our high- T data allow us to calculate the intrinsic anharmonicity (a_i) for Raman-active modes, which can be defined as

$$a_i = \left(\frac{\partial \ln \nu_i}{\partial T} \right)_V. \quad (4)$$

According to Gillet et al. (1997),

$$\int_{T_0}^T a_i dT = \ln \nu(V, T) - \ln \nu(V, P_0) = \Delta \ln \nu_{th} \quad (5)$$

where the first term at the right side can be directly obtained from our data, and the second term at the right side can be obtained by extrapolating high- P results to the thermal expansion regime as shown in Figures 7a–7d. For the second term, we used results from a high- P Raman study on natural OEn by Lin (2003), which fit the P -induced frequency shifts to

$$\nu_i(V, P) = \nu_{0 \text{ GPa}} + A_P P + B_P P^2. \quad (6)$$

We shifted ($\nu_{0 \text{ GPa}}$) in Lin's (2003) fit to our measured frequencies at 1 bar and 300 K to match the ν 's between compression and heating data at the reference state. The shifts do not exceed 3 cm^{-1} . The result was extrapolated to the thermal expansion regime using the Birch-Murnaghan equation (Birch 1978). The bulk modulus and pressure derivative bulk modulus of OEn were obtained from Hugo-Jones and Angel (1994). Since the extrapolation is necessary only to $V/V_0 \approx 1.04$, we believe uncertainties from the extrapolation may not be significant.

Except for n_1 and n_3 , all the OEn modes we traced to high T showed a linear relationship between $\Delta \ln \nu_{th}$ and T (Figs. 7e–7i), as also found in Fo (Gillet et al. 1997). Therefore, we can obtain a_i from the slope of the trend in Figures 7g–7i for each mode (Table 1). As shown in Figures 7e and 7f, even after the subtraction of volume effects, $\ln \nu(V, P_0)$, severe non-linear trends remain for n_1 and n_3 (Figs. 7e and 7h). Therefore, we fit the trends in n_1 and n_3 to

$$\Delta \ln \nu_{th} = \ln \nu(V, T) - \ln \nu(V, P_0) = a_i \Delta T + a_i' T^2 + a_i'' T^3 \quad (7)$$

where $\Delta T = T - 300 \text{ K}$. The fit results are provided in Table 1.

Raman scattering of high- T phase

Significant changes were detected between 70 and 500 cm^{-1} in the T range of 1480 – 1500 K , indicating a phase transition (Figs. 4 and 5). The measured T for the phase transition is consistent with a previous study with a starting material predominantly OEn (Smyth 1974). The sample used in run 4 did not undergo the phase transformation until 1550 K . The possible reasons for the discrepancy with other runs are discussed above.

Most of the changes associated with the phase transformation occurred within a few minutes during both heating and cooling. However, n_1 did not disappear completely at temperatures higher than the transition T in run 2, and n_8 did not split in run 5 until

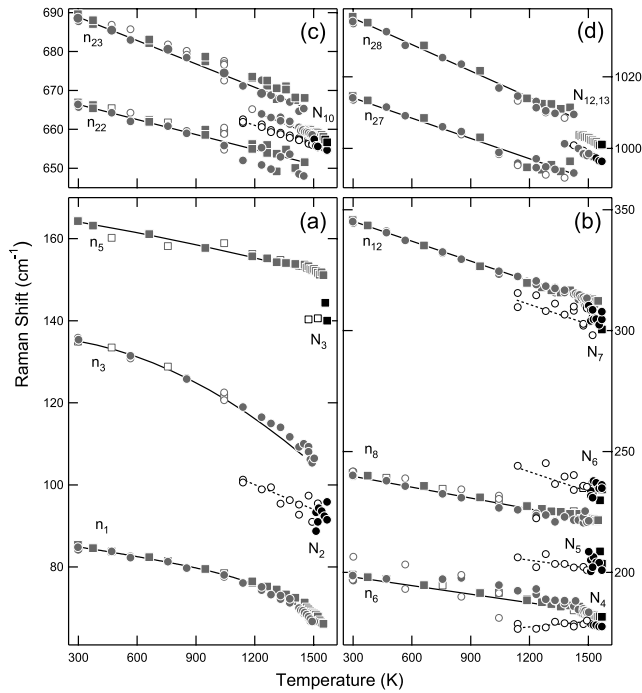


FIGURE 6. Frequencies of major Raman-active phonon modes of OEn (gray symbols) and high- T phase (black symbols). The circles represent data points from run 2 and 5. The squares are the data points from run 4. The open and closed symbols represent data points measured during cooling and heating, respectively. The solid and dashed lines are polynomial fits of the heating (shown also in Table 1) and cooling data points, respectively.

higher T . Smyth (1974) reported that the high- T transition from a dominantly OEn sample is sluggish and requires several days of heating at 1473 K. Yang and Ghose (1995) found that the transition occurs at 1273 K after heating for 9 h. Because we only heated for a few hours, a higher T for the transition in our study may be due to kinetics.

For the high- T phase, a total of 9–10 modes were identified. Mode N_1 is very weak and appears to be related to n_1 , with no change in frequency across the phase transition, and disappears with further heating (Fig. 4). Therefore, this mode may be due to the survival of the n_1 of OEn into the stability field of the high- T

phase due to kinetic effects.

The N_2 mode is the most prominent feature after the phase transition. Mode N_3 is observed only in run 4, and appears related to n_5 , which is also found only in run 4 (Figs. 5 and 6a). The frequency of n_6 dropped by 5 cm^{-1} at the phase transition and we assigned it to N_4 after the phase transition (Fig. 6). Mode n_8 appears to split into two modes, N_5 and N_6 , at the phase transition (Fig. 6b). The mode frequency of n_{12} decreased by 5 cm^{-1} at the phase transition (N_7).

Resolution of the two doublets ($n_{22,23}$ and $n_{27,28}$) in OEn becomes less clear after the phase transition (N_{10} and $N_{12,13}$, respectively) (Figs. 4 and 5). The full-width at half maximum (FWHM) was plotted for these peaks across the phase transition (Fig. 8). A discontinuous drop in the peak width at the phase transition occurs for N_{10} , indicating that N_{10} is a single peak. In addition, while the high- T phase metastably persists during cooling, the width of N_{10} remains smaller than that of $n_{22,23}$. Furthermore, the mode frequency of N_{10} decreases slightly by 2 cm^{-1} relative to mode $n_{22,23}$ at the phase transition. The width of $N_{12,13}$ is continuous across the phase transformation, indicating that it remains a doublet. N_{12} and N_{13} can be resolved by peak fitting upon cooling, below 1273 K.

We also monitored the sample through a video microscope across the phase transition temperature and found that the sample changed from transparent to milky-white because of intense micro-fracturing at the phase transition temperature.

Upon cooling, a marked hysteresis in the transition T was observed. The sample transformed from the high- T phase to OEn between 1173 and 1073 K in runs 2 and 5. In run 4, the sample transformed back to OEn between 1523 and 1473 K. As discussed above, the higher transition temperature in run 4 appears to be an experimental artifact.

The spectra attained at room T after heating show some differences from the pre-heating room- T spectra (Figs. 4 and 5). Mode n_1 decreased in intensity by about a factor of 2 in runs 2 and 5 (Fig. 4). Mode n_2 increased in relative intensity and showed a change in its frequency, shifting up 3.5 cm^{-1} after cooling. Mode n_8 broadened significantly after cooling and shifted up by 2 cm^{-1} in frequency. Mode n_{24} was not present before heating and was only visible in the cooled room- T spectrum.

Smyth (1974) has shown that slow cooling of PEn results in

TABLE 1. Selected vibrational mode frequencies of OEn measured at 300 K and 1 bar (ν_{obs})

	ν_{obs}	This study						Lin (2003)		
		ν_{0K} (cm^{-1})	$A_T \times 10^3$ (cm^{-1}/K)	$B_T \times 10^5$ ($\text{cm}^{-1}/\text{K}^2$)	$a_1 \times 10^5$ (K^{-1})	$a'_1 \times 10^7$ (K^{-2})	$a''_1 \times 10^{10}$ (K^{-3})	$\nu_{0\text{GPa}}$ (cm^{-1})	A_P ($\text{cm}^{-1}/\text{GPa}$)	$B_P \times 10^2$ ($\text{cm}^{-1}/\text{GPa}^2$)
n_1	85	82.4(10)	8.9(23)	-1.3(1)*	-29(9)	5(1)	-2.3(4)	83.4	2.36	-12.89
n_3	136	136.4(18)	-1.0(43)	-1.2(2)*	-13(15)	2(2)	-1.2(6)	134.3	4.77	-15.47
n_5	164	167.3(4)	-9.9(3)†,§		-2.2(2)			166.7	2.58	-10.03
n_6	198	202.6(3)	-11.9(2)‡,§		-4.5(1)			196.9	1.24	-5.73
n_8	240	244.8(7)	-15.5(5)		-6.2(2)			238.2	1.96	-6.75
n_{12}	345	353.0(4)	-27.0(3)		-3.0(1)			343.5	6.93	-16.22
n_{22}	666	670.9(9)	-14.4(9)		-0.8(1)			663.8	3.87	-5.03
n_{23}	689	694.9(7)	-19.3(7)		-1.5(1)			686.1	3.83	-6.90
n_{27}	1014	1020.3(7)	-19.5(7)		-0.25(7)			1011.3	6.79	-16.14
n_{28}	1036	1043.5(6)	-24.4(6)		-0.86(6)			1032.9	6.28	-13.39

Notes: Vibrational frequencies were fit to Equation 3 (ν_{0K} , A_T , and B_T). The trends observed in Figures 7e–7i were fit to Equation 7 (a_i , a'_i , and a''_i). Fit results for pressure-induced mode frequency shifts were obtained from Lin (2003) (Eq. 6: $\nu_{0\text{GPa}}$, A_P , and B_P).

* Fit the data points only from runs 2 and 5.

† Observed only in run 4.

‡ Well resolved only in run 4.

§ Exclude data points at $T > 1450$ K due to a change in the rate frequency decrease above the temperature.

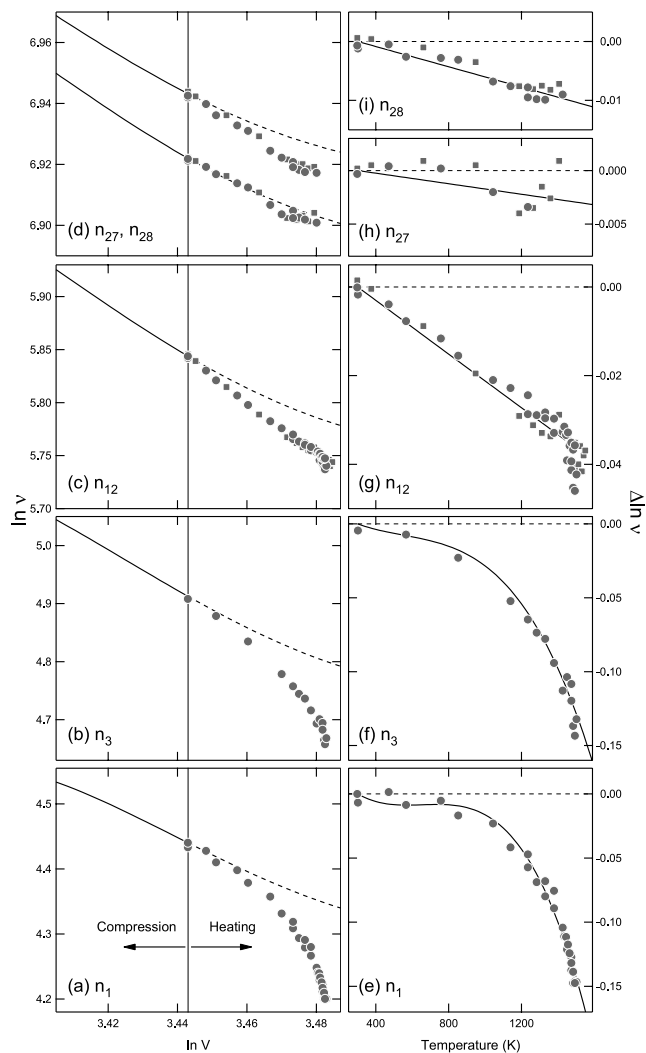


FIGURE 7. The $\ln V - \ln \nu$ (**a–d**) and $\ln \nu_{th} - T$ (**e–i**) plots for selected Raman-active OEn modes. These plots were made to obtain intrinsic mode anharmonicity following the method of Gillet et al. (1997). The gray symbols are our high- T measurements (circles are from runs 2 and 5; and squares are from run 4). The solid lines in **a–d** were obtained from P -induced mode shifts of OEn from Lin (2003) and the dashed lines in **a–d** are the extrapolation of the solid lines to the thermal expansion regime. The solid curves in **e–i** are the fit results for the data (Eq. 7). The slopes in **a–d** are related to the mode Grüneisen parameters, and the slopes in **e–i** are related to the intrinsic mode anharmonicity, a_i . The fit results are also presented in Table 1. The vertical lines in **a–d** represent volume at a reference state, 300 K and 1 bar.

a mixture of LTCEn and OEn, whereas fast cooling results in LTCEn. The frequency shift and intensity increase of n_2 and n_8 are consistent with the appearance of LTCEn during cooling. Furthermore, the appearance of n_{24} can be explained by the existence of LTCEn in the quench product. These appear to be permanent changes as they remain in the spectrum measured 6 months after the heating cycle.

DISCUSSION

Intrinsic mode anharmonicity has also been studied for Mg_2SiO_4 -forsterite (Fo), which is another important upper

mantle mineral, through the same spectroscopic approach (Gillet et al. 1991, 1997). It is of interest to compare our results on OEn to Fo. Intrinsic mode anharmonicity has a negative sign in OEn for all the modes we reliably traced with heating, which was also found in Fo (Gillet et al. 1997). In general, the low-frequency lattice modes of OEn, such as n_{12} in Figure 7g, have greater anharmonicity than the Si-O stretching vibration, n_{27} and n_{28} in Figures 7h and 7i (Table 1). The same trend was also found in Fo (Gillet et al. 1991). However, the a_i values of the lattice modes between 200 and 600 cm^{-1} are generally greater in magnitude in OEn than in Fo. For the a_i values of the Si-O stretching vibration, the magnitudes are significantly smaller in OEn than in Fo. The latter observation is perhaps related to the different SiO_4 tetrahedral linkage in these two minerals: SiO_3 chain in OEn and isolated SiO_4 tetrahedra in Fo.

Another important difference is in the strong non-linear trends found in the n_1 and n_3 modes of OEn (Figs. 6 and 7). Although Raman measurements were conducted to much higher T (2000 K) for Fo (Gillet et al. 1997), none of the Raman-active modes of Fo showed such non-linear decrease in vibrational frequency. It is also notable that even after subtracting volume effects through Equation 5, the non-linear trends remain for both n_1 and n_3 (Figs. 7e and 7f), indicating that the non-linear trends may not be due simply to thermal expansion. Because Equation 5 subtracts both volume effects and intrinsic pressure effects from high-temperature frequency shifts, it cannot be ruled out that intrinsic pressure effects may contribute to the trends shown in Figures 7e and 7f. However, because large non-linear

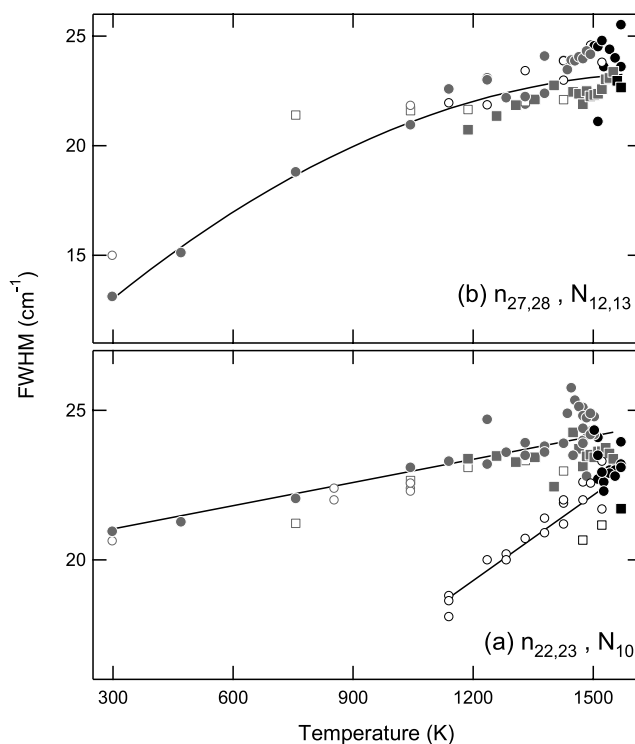


FIGURE 8. The full-width at half maxima (FWHM) of $n_{22,23}$ and N_{10} (**a**), and $n_{27,28}$ and $N_{12,13}$ (**b**) at high T . The solid lines are the polynomial fittings of the data points. The other notations are the same as those in Figure 6.

frequency decreases are obvious in the frequency vs. T plot for n_1 and n_3 (Fig. 6), temperature should be the dominant factor for the non-linear trends.

Intrinsic anharmonicity can be also examined by inspecting the departure of isochoric heat capacity (C_V) from the Dulong-Petit limit. We calculated C_V from the recently published isobaric heat capacity (C_P) of OEn measured up to 1390 K (Thiéblot et al. 1999) and thermoelastic data measured to temperatures over 1000 K (Jackson et al. 2003, 2007) using the following equation:

$$C_V = C_P - TV\alpha^2 K_T \quad (8)$$

where α is thermal expansion parameter and K_T is isothermal bulk modulus. We found that the C_V of OEn converges to the Dulong-Petit limit above 1100 K, and the difference between C_V and $3nR$ does not exceed 1%. This leads us to conclude that intrinsic anharmonicity contribution should be small in OEn. Therefore, the strong temperature dependence of a_i for n_1 and n_3 (Figs. 7e and 7f) could be a result of highly localized change in the crystal structure of OEn with heating. It is notable that the non-linear trends in n_1 and n_3 begin at much lower temperatures than the transition T .

Our high- T spectra of En also provide some insights into the crystal structure of the high- T phase. The crystal structure of protoenstatite (PEn) was successfully solved by single-crystal XRD for $\text{Li}_{0.3}\text{Sc}_{0.3}\text{Mg}_{1.4}\text{Si}_2\text{O}_6$ quenched to ambient T (Smyth and Ito 1977). Single-crystal Raman spectroscopy has been also performed for $\text{Li}_{0.3}\text{Sc}_{0.3}\text{Mg}_{1.4}\text{Si}_2\text{O}_6$ at room T (Ghose et al. 1994). Due to the thermal effects on the peak width and frequency in our Raman scattering, and dopant cations and their site orderings in $\text{Li}_{0.3}\text{Sc}_{0.3}\text{Mg}_{1.4}\text{Si}_2\text{O}_6$ -PEn, direct comparisons are difficult. Nevertheless, the overall spectra are very similar. The most prominent similarities can be found in the frequency and relative intensity of N_2 , N_7 , N_8 , N_{10} , and $N_{12,13}$ (see also Fig. 2 in Ghose et al. 1994), suggesting that the high- T phase we observed likely has the PEn structure.

In addition, molecular dynamic simulations on PEn (Ghose et al. 1994; Choudhury et al. 1998) predicted an intense mode at 104 cm^{-1} , which can be related to N_2 in our high- T Raman spectra (Figs. 4 and 5). The frequency of N_2 at 1143 K is 101 cm^{-1} , which is close to the predicted value. Furthermore, the frequency of this mode also agrees with an intense low-frequency mode observed in metastably quenched PEn at room T (Reynard et al. 2008). Choudhury et al. (1998) related this mode to the n_1 of OEn, which is from translations and rotations of the SiO_3 chains, and translations of Mg. The OEn \rightarrow PEn transition involves a change in the octahedral-layer sequence, i.e., skewness changes (Cameron and Papike 1980). Therefore, the Mg-O sublattice in En should undergo reconstructive changes. As discussed above, n_1 shows a strong non-linear temperature-induced frequency shift from temperatures well below the transition T , suggesting that the structural changes related to this mode may begin at low temperatures.

A single-crystal XRD study (Yang and Ghose 1995) found that SiO_3 chains with a larger kink angle in OEn begin to straighten rapidly at a much lower T than the transition T , followed by abrupt increases in the kink angles in both chains to

the same magnitude at the transition T . Because n_1 is also related to the rotations of the SiO_3 chain (Choudhury et al. 1998), its non-linear frequency shift observed well below the transition T in our study may be related to the structural changes observed in the single-crystal XRD study.

The N_{10} mode was assigned to the symmetric stretching vibrations of the bridging oxygen atom in the SiO_3 chain (Choudhury et al. 1998). A molecular dynamics simulation related the N_{10} mode to the n_{22} and n_{23} modes of OEn (Choudhury et al. 1998). Above we showed that the $n_{22}+n_{23}$ doublet becomes a singlet (N_{10}) after the phase transition. This is also in agreement with the observation of a singlet in the same frequency range in metastably quenched PEn (Reynard et al. 2008). It is notable that across the OEn \rightarrow PEn transition, two symmetrically distinct SiO_3 chains become identical, which is reflected by the merging of n_{22} and n_{23} in OEn to N_{10} .

From the molecular dynamics simulation, n_{27} and n_{28} are related to the stretching of the Si-O nonbridging O atoms in two different tetrahedral chains (Choudhury et al. 1998). Because two different tetrahedral chains are equivalent in PEn, n_{27} and n_{28} may become a singlet after the OEn \rightarrow PEn transition. However, we observed that these modes remain separated ($N_{12,13}$) even after the phase transition (Fig. 8). It is possible that each of these modes are sensitive to two different nonbridging O atoms in an SiO_4 tetrahedron. In that case, no peak merge is expected for these modes even after the OEn \rightarrow PEn transition, which is consistent with our observation. We also note that these modes were observed as separate peaks in a metastably quenched PEn crystal (Reynard et al. 2008). Therefore, our observations are consistent with a phase transition from OEn to PEn at high temperature and 1 bar.

Finally, our in situ Raman observation provides some insights into the interpretation of the recent Brillouin study (Jackson et al. 2004). We found that a low-frequency phonon mode (n_1), which is related to translations and rotations of the SiO_3 chains, and translations of Mg, shows a severe softening well below the transition T . In a similar temperature range, elastic softening was observed in Brillouin spectroscopy of OEn (Jackson et al. 2004). Therefore, these two observations combined with the single-crystal XRD study (Yang and Ghose 1995) may support changes in the crystal structure of OEn occurring at temperatures well below the phase transition temperature.

ACKNOWLEDGMENTS

We thank A. Hofmeister and an anonymous reviewer for helpful suggestions and discussions. R.Z. was supported by the Leslie C. Patron Undergraduate Research Fund. Construction of the laser Raman system was supported by the National Science Foundation (NSF), EAR0337156, to S.-H.S. Raman measurements were supported by the NSF (EAR0337005) to S.-H.S. Some preliminary measurements were conducted by R. Lamm.

REFERENCES CITED

- Bernardez, L., McCarty, K.F., and Yang, N. (1992) In situ Raman spectroscopy of diamond during growth in a hot filament reactor. *Journal of Applied Physics*, 72, 2001–2005.
- Birch, F. (1978) Finite strain isotherm and velocities for single-crystal and polycrystalline NaCl at high pressures and 300 K. *Journal of Geophysical Research*, 83, 1257–1268.
- Cameron, M. and Papike, J. J. (1980) Crystal chemistry of silicate pyroxenes. In C.T. Prewitt, Ed., *Pyroxenes*, 7, p. 5–92. Reviews in Mineralogy, Mineralogical Society of America, Chantilly, Virginia.
- Catali, K., Shim, S.-H., and Prakapenka, V.B. (2008) A crystalline-to-crystalline

- phase transition in Ca(OH)₂ at 8 GPa and room temperature. *Geophysical Research Letters*, 35, L05312.
- Chopelas, A. (1999) Estimates of mantle relevant Clapeyron slopes in the MgSiO₃ system from high-pressure spectroscopic data. *American Mineralogist*, 84, 233–244.
- Choudhury, N., Ghose, S., Pal Chowdhury, C., Loong, C.K., and Chaplot, S.L. (1998) Lattice dynamics, Raman spectroscopy, and inelastic neutron scattering of orthoenstatite Mg₂Si₂O₆. *Physical Review B*, 58, 756–765.
- Eremets, M. (1996) *High Pressure Experimental Methods*, 408 p. Oxford University Press, U.K.
- Exarhos, G.J. and Schaaf, J.W. (1991) Raman scattering from boron nitride coatings at high temperatures. *Journal of Applied Physics*, 69, 2543–2548.
- Fayette, L., Marcus, B., Mermoux, M., Rosman, N., Abello, L., and Lucazeau, G. (1994) In situ Raman spectroscopy during diamond growth in a microwave plasma reactor. *Journal of Applied Physics*, 76, 1604–1608.
- Ghose, S., Choudhury, N., Chaplot, S.L., Pal Chowdhury, C., and Sharma, S.K. (1994) Lattice dynamics and Raman spectroscopy of protoenstatite Mg₂Si₂O₆. *Physics and Chemistry of Minerals*, 20, 469–477.
- Gillet, P., Guyot, F., and Malezieux, J.-M. (1989) High-pressure, high-temperature Raman spectroscopy of Ca₂GeO₄ (olivine form): some insights on anharmonicity. *Physics of the Earth and Planetary Interiors*, 58, 141–154.
- Gillet, P., Richet, P., Guyot, F., and Fiquet, G. (1991) High-temperature thermodynamic properties of forsterite. *Journal of Geophysical Research*, 96, 11805–11816.
- Gillet, P., Guyot, F., Price, G.D., Tournier, B., and Cleach, A.L. (1993) Phase changes and thermodynamic properties of CaTiO₃. Spectroscopic data, vibrational modelling and some insights on the properties of MgSiO₃ perovskite. *Physics and Chemistry of Minerals*, 20, 159–170.
- Gillet, P., Daniel, I., and Guyot, F. (1997) Anharmonic properties of Mg₂SiO₄-forsterite measured from the volume dependence of the Raman spectrum. *European Journal of Mineralogy*, 9, 255–262.
- Gillet, P., Hemley, R.J., and McMillan, P.F. (1998) Vibrational properties at high pressures and temperature. In R.J. Hemley, Ed., *Ultrahigh-Pressure Mineralogy*, 37, p. 525–590. *Reviews of Mineralogy, Mineralogical Society of America, Chantilly, Virginia*.
- Goncharov, A.F. and Crowhurst, J.C. (2005) Pulsed laser Raman spectroscopy in the laser-heated diamond anvil cell. *Review of Scientific Instruments*, 76, 063905.
- Herchen, H. and Cappelli, M.A. (1991) First-order Raman spectrum of diamond at high temperatures. *Physical Review B*, 43, 11740–11744.
- Hugo-Jones, D.A. and Angel, R.J. (1994) A compressional study of MgSiO₃ orthoenstatite up to 8.5 GPa. *American Mineralogist*, 79, 405–410.
- Hustoft, J., Shim, S.-H., Kubo, A., and Nishiyama, N. (2008) Raman spectroscopy of CaIrO₃ postperovskite up to 30 GPa. *American Mineralogist*, 93, 1654–1658.
- Ita, J. and Stixrude, L. (1992) Petrology, elasticity and composition of the mantle transition zone. *Journal of Geophysical Research*, 97, 6842–6866.
- Jackson, J.M., Palko, J.W., Andrault, D., Sinogeikin, S.V., Lakshtanov, D.L., Wang, J., Bass, J.D., and Zha, C.-S. (2003) Thermal expansion of natural orthoenstatite to 1473 K. *European Journal of Mineralogy*, 15, 469–473.
- Jackson, J.M., Sinogeikin, S.V., Carpenter, M.A., and Bass, J.D. (2004) Novel phase transition in orthoenstatite. *American Mineralogist*, 89, 239–245.
- Jackson, J.M., Sinogeikin, S.V., and Bass, J.D. (2007) Sound velocities and single-crystal elasticity of orthoenstatite to 1073 K at ambient pressure. *Physics of the Earth and Planetary Interiors*, 161, 1–12.
- Knittle, E. and Jeanloz, R. (1987) Synthesis and equation of state of (Mg,Fe)SiO₃ perovskite to over 100 gigapascals. *Science*, 235, 668–670.
- LaPlant, F., Laurence, G., and Ben-Amotz, D. (1996) Theoretical and experimental uncertainty in temperature measurement of materials by Raman spectroscopy. *Applied Spectroscopy*, 50, 1034–1038.
- Laserna, J.J. (1996) *Modern Techniques in Raman Spectroscopy*, 446 p. Wiley, New York.
- Lin, C.-C. (2003) Pressure-induced metastable phase transition in orthoenstatite (MgSiO₃) at room temperature: A Raman spectroscopic study. *Journal of Solid State Chemistry*, 174, 403–411.
- (2004) Pressure-induced polymorphism in enstatite (MgSiO₃) at room temperature: clinoenstatite and orthoenstatite. *Journal of Physics and Chemistry of Solids*, 65, 913–921.
- McCarty, K.F. (1990) Investigations of materials at high temperatures using Raman spectroscopy. *High Temperature Science*, 26, 19–30.
- McMillan, P.F. and Hofmeister, A.M. (1988) Infrared and Raman spectroscopy. In F.C. Hawthorne, Ed., *Spectroscopic Methods in Mineralogy and Geology*, 18, p. 99–159. *Reviews of Mineralogy, Mineralogical Society of America, Chantilly, Virginia*.
- Miyake, A., Shimobayashi, N., and Kitamura, M. (2004) Isosymmetric structural phase transition of orthoenstatite: Molecular dynamic simulation. *American Mineralogist*, 89, 1667–1672.
- Mulac, A.J., Flower, W.L., Hill, R.A., and Aeschliman, D.P. (1978) Pulsed spontaneous Raman scattering technique for luminous environments. *Applied Optics*, 17, 2695–2699.
- Perrotta, A.J. and Stephenson, D.A. (1965) Clinoenstatite: high-low inversion. *Science*, 148, 1090–1091.
- Reynard, B., Bass, J.D., and Jackson, J.M. (2008) Rapid identification of steatite-enstatite polymorphs at various temperatures. *Journal of the European Ceramic Society*, 28, 2459–2462.
- Ringwood, A.E. (1975) *Composition and Petrology of the Earth's Mantle*, 672 p. McGraw-Hill, New York.
- Sharma, S.K. (1989) *Applications of Advanced Raman Spectroscopic Techniques in Earth Sciences*, p. 513–568. Elsevier, Amsterdam.
- Shim, S.-H., Kubo, A., and Duffy, T.S. (2007) Raman spectroscopy of perovskite and post-perovskite phases of MgGeO₃ to 123 GPa. *Earth and Planetary Science Letters*, 260, 166–178.
- Shimobayashi, N. and Kitamura, M. (1993) Phase transition of orthoenstatite to high-clinoenstatite: In situ TEM study at high temperatures. *Mineralogical Journal*, 16, 416–426.
- Simon, P., Moulin, B., Buixaderas, E., Raimboux, N., Herault, E., Chazallon, B., Cattet, H., Magoner, N., Oswald, J., and Hocrelle, D. (2003) High temperatures and Raman scattering through pulsed spectroscopy and CCD detection. *Journal of Raman Spectroscopy*, 34, 497–504.
- Slotznick, S.P. and Shim, S.-H. (2008) In situ Raman spectroscopy measurements of MgAl₂O₄ spinel up to 1400 °C. *American Mineralogist*, 93, 470–476.
- Smyth, J.R. (1974) Experimental study on the polymorphism of enstatite. *American Mineralogist*, 59, 345–352.
- Smyth, J.R. and Ito, J. (1977) The synthesis and crystal structure of a magnesium-lithium-scandium protopyroxene. *American Mineralogist*, 62, 1252–1257.
- Stixrude, L., Hemley, R.J., Fei, Y., and Mao, H.K. (1992) Thermoelasticity of silicate perovskite and magnesiowüstite and stratification of the Earth's mantle. *Science*, 257, 1099–1101.
- Thiéblot, L., Têqui, C., and Richet, P. (1999) High-temperature heat capacity of grossular (Ca₃Al₂Si₂O₁₂), enstatite (MgSiO₃), and titanite (CaTiSiO₅). *American Mineralogist*, 84, 848–855.
- Weber, W.H. and Merlin, R. (2000) *Raman Scattering in Materials Science*, 492 p. Springer, New York.
- Yang, H. and Ghose, S. (1995) High temperature single crystal X-ray diffraction studies of the ortho-proto phase transition in enstatite, Mg₂Si₂O₆ at 1360 K. *Physics and Chemistry of Minerals*, 22, 300–310.

MANUSCRIPT RECEIVED FEBRUARY 5, 2009

MANUSCRIPT ACCEPTED JULY 7, 2009

MANUSCRIPT HANDLED BY BRIGITTE WOPENKA